# The Shape of (486958) Arrokoth

Simon B. Porter,[1] Kelsi N. Singer,[1] Paul M. Schenk,[2] Anne J. Verbiscer,[3] Susan D. Benecchi,[4]
John R. Spencer,[1] Joel W. Parker,[1] Pontus Brandt,[5] and S. Alan Stern[1]

[1]*Southwest Research Institute, 1301 Walnut St, Suite 400, Boulder, CO 80302, USA*
[2]*Lunar and Planetary Institute, 3600 Bay Area Blvd., Houston, TX 77058, USA*
[3]*Department of Astronomy, University of Virginia, P.O. Box 400325, Charlottesville, VA, 22904, USA*
[4]*Planetary Science Institute, 1700East Fort Lowell, Suite 106, Tucson, AZ, 85719, USA*
[5]*Johns Hopkins University Applied Physics Laboratory, Laurel, MD, USA*

## ABSTRACT

Here we present an updated shape model of (486958) Arrokoth, the bilobate Kuiper Belt Object (KBO) which the NASA New Horizons spacecraft flew past in 2019. This updated shape model uses all of the resolved images of Arrokoth obtained by the New Horizons LOng Range Reconnaissance Imager (LORRI). We developed an updated shape modeling algorithm which allowed the shape and rotational pole of Arrokoth to be fit to much better quality with an efficient use of GPU-accelerated features. The resulting model of Arrokoth's contact binary shape is significantly thicker and of larger volume than the one previously published immediately after the flyby by Spencer et al (2020). We show that Arrokoth's smaller lobe Weeyo is roughly spherical in shape, while the larger lobe Wenu is more flattened, with the volume ratio between the lobes being roughly 2:1. Owing to Wenu's oblate shape, Arrokoth's rotational lightcurve would have significantly lower mean reflectance when viewed from subobserver latitudes that would have shown lightcurve variation. We discuss the impact this may have on estimates of the frequency of contact binaries in the Kuiper Belt. We also discuss the implications of this shape for the formation of Arrokoth, particularly in the context of the Streaming Instability.

## 1. INTRODUCTION

On January 1, 2019, NASA's New Horizons spacecraft flew about 3500 km from the (486958) Arrokoth, a Cold Classical Kuiper Belt Object (KBO), making it the farthest solar system object from the Sun to be studied up close by a spacecraft (Stern et al. 2019). The Kuiper Belt was named after the predictions of Kuiper (1974) of a large comet belt beyond Neptune, which had been first predicted by Edgeworth (1949), and was first confirmed to exist with the discovery of 1992 $QB_1$, now (15760) Albion (Jewitt & Luu 1993). Albion is a roughly 100 km long object that has a mean distance from the Sun of about 44 AU in a near-circular ($e < 0.1$), low inclination orbit (Benecchi et al. 2011). These characteristics made Albion not just the first small KBO to be discovered, but also the archetype for the specific class of "Cold Classical KBOs" (CCKBOs) that appear to be in orbits which were not significantly perturbed during the giant planet migration phase (Elliot et al. 2005), thus making them effectively fossils of the early stages of planet formation (Tsiganis et al. 2005). This lack of migration has allowed the CCKBOs to have suffered far fewer impacts than other populations beyond Neptune (Greenstreet et al. 2019), and the lack of impacts is proven out with the relatively high fraction of CCKBOs that are seen to be very wide (loosely-bound) binaries (Grundy et al. 2019). Indeed, the overall binary fraction for the CCKBOs is quite high, at 21% detectable as binaries with the resolution to the Hubble Space Telescope (HST) Wide Field Camera 3 (WFC3) instrument (1000 km, Porter et al, 2024, in press), and more tighter CCKBO binaries detected with an occultation (350 km; Leiva et al. 2020) and two with direct imaging by the New Horizons spacecraft (200 km; Weaver et al. 2022). Ground-based lightcurve studies showed that at least half of CCKBOs could be contact binaries (Thirouin & Sheppard 2019), though lightcurves can only be used to detect the fraction of KBOs that are roughly equator-on as seen from Earth (Showalter et al. 2021).

**Table 1.** Description of LORRI image sequences used in this analysis.

| REQID[a] | Observation Date | Exposure Time (s) | Num. Img.[b] | Dist (km)[c] | Sol. Phase[d] | m/px Res.[e] |
|---|---|---|---|---|---|---|
| APROTNAV_L1_2018365A | 2018-12-31 18:13:13.719 | 0.1506 | 6 | 589111 | 11.701° | 2970.3 |
| APROTNAV_L1_2018365B | 2018-12-31 18:46:13.719 | 0.1506 | 6 | 560529 | 11.699° | 2826.2 |
| APROTNAV_L1_2018365C | 2018-12-31 19:23:13.719 | 0.1506 | 6 | 528483 | 11.697° | 2664.6 |
| APROTNAV_L1_2018365D | 2018-12-31 20:00:13.719 | 0.1506 | 6 | 496436 | 11.695° | 2503.1 |
| APROTNAV_L1_2018365E | 2018-12-31 20:38:13.719 | 0.1506 | 6 | 463524 | 11.692° | 2337.1 |
| APROTNAV_L1_2018365F | 2018-12-31 21:28:13.719 | 0.1506 | 6 | 420218 | 11.687° | 2118.8 |
| APROTNAV_L1_2018365G | 2018-12-31 22:01:53.719 | 0.1506 | 6 | 391059 | 11.684° | 1971.7 |
| APROTNAV_L1_2018365H | 2018-12-31 22:46:13.719 | 0.1506 | 6 | 352662 | 11.679° | 1778.1 |
| APROTNAV_L1_2018365I | 2018-12-31 23:26:13.719 | 0.1506 | 6 | 318018 | 11.674° | 1603.5 |
| APROTNAV_L1_2018365J | 2018-12-31 23:46:28.719 | 0.1506 | 6 | 300480 | 11.671° | 1515.0 |
| APROTNAV_L1_2019001A | 2019-01-01 00:07:59.719 | 0.1506 | 6 | 281845 | 11.667° | 1421.1 |
| APROTNAV_L1_2019001B | 2019-01-01 00:29:30.719 | 0.1506 | 6 | 263210 | 11.663° | 1327.1 |
| APROTNAV_L1_2019001C | 2019-01-01 00:51:01.719 | 0.1506 | 6 | 244575 | 11.659° | 1233.2 |
| APROTNAV_L1_2019001D | 2019-01-01 01:12:32.719 | 0.1506 | 6 | 225941 | 11.655° | 1139.2 |
| APROTNAV_L1_2019001E | 2019-01-01 01:34:03.719 | 0.1506 | 6 | 207307 | 11.650° | 1045.3 |
| APROTNAV_L1_2019001F | 2019-01-01 01:55:34.719 | 0.1506 | 6 | 188674 | 11.645° | 951.3 |
| APROTNAV_L1_2019001G | 2019-01-01 02:17:05.719 | 0.1506 | 6 | 170041 | 11.640° | 857.4 |
| APMAP_L1_2019001__stare1 | 2019-01-01 02:45:44.553 | 0.1506 | 6 | 145235 | 11.635° | 732.3 |
| APMAP_L1_2019001__mosaic | 2019-01-01 02:59:45.553 | 0.1506 | 4 | 133098 | 11.633° | 671.1 |
| APMAP_L1_2019001__stare2 | 2019-01-01 03:08:44.553 | 0.1506 | 6 | 125320 | 11.632° | 631.9 |
| APRETARG_L1_2019001 | 2019-01-01 03:21:07.553 | 0.1506 | 12 | 114599 | 11.633° | 577.8 |
| APROTNAV_L1_2019001I | 2019-01-01 03:26:25.053 | 0.1506 | 6 | 110018 | 11.634° | 554.7 |
| APROTNAV_L1_2019001J | 2019-01-01 03:43:15.053 | 0.1506 | 6 | 95447 | 11.643° | 481.2 |
| APROTNAV_L1_2019001K | 2019-01-01 04:04:32.053 | 0.1506 | 6 | 77028 | 11.675° | 388.4 |
| CA01-MAP_L1_2019001 | 2019-01-01 04:22:49.053 | 0.1506 | 49 | 61213 | 11.751° | 308.6 |
| CA02-MAP_L1_2019001 | 2019-01-01 04:44:17.115 | 0.0256 | 7 | 42664 | 12.039° | 215.1 |
| CA04-MAP_L1_2019001 | 2019-01-01 05:01:20.078 | 0.1006 | 31 | 27974 | 12.907° | 141.0 |
| CA05-MAP_L1_2019001 | 2019-01-01 05:14:33.115 | 0.0256 | 7 | 16681 | 15.694° | 84.1 |
| CA06-PREALLOC_L1_2019001 | 2019-01-01 05:26:54.615 | 0.0256 | 6 | 6622 | 32.585° | 33.4 |
| CA07-LIMB_L4_2019001 | 2019-01-01 05:42:42.028 | 0.2006 | 13 | 8818 | 152.333° | 177.9 |

[a] Image sequence identifier; the prefix KELR_MU69_ has been removed for clarity

[b] Number of raw images used for the final stacked image

[c] New Horizons-Arrokoth distance in kilometers

[d] Sun-Arrokoth-New Horizons Solar Phase angle in degrees

[e] Original image ground pixel scale in meters per pixel, not taking into account any smear

Even before New Horizons' flyby of Arrokoth, these discoveries led to the theory that all CCKBOs may have initially formed as separated binaries (Fraser et al. 2017), with many later either being split or merging into contact binaries. A formation theory that supports the concept of (nearly) all CCKBOs forming as binary objects is the Streaming Instability (SI; Nesvorný et al. 2019). The SI theory postulates that the primary mechanism that formed planetesimals in the outer proto-Solar disk was gas drag causing dust to clump into linear "streams", which then gravitationally collapse into solid bodies (see Youdin & Johansen 2007; Carrera et al. 2017; Abod et al. 2019, for far more details). A key factor of SI formation is that it is fast, too fast to allow gas drag to bleed away much angular momentum

from the collapsing dust clouds (Youdin & Johansen 2007). The rapid gravitational collapse of the solid material while preserving angular momentum means that SI directly forms binary KBOs from the disk (Nesvorný et al. 2019), without any need for later binary capture (e.g. Goldreich et al. 2002). Because of this rapid collapse, SI can even form triple or higher systems (Nesvorný et al. 2019), though only one triple KBO is known to exist (Lempo; Benecchi et al. 2010) with at least one more suspected from orbital analysis (Altjira; Nelsen et al. 2024). Importantly, binaries formed from the SI process should have identical composition for both bodies, and show a preference for prograde orbits, as this is the direction of the net angular momentum vector favored by gravitational shear of the streams in the SI (Nesvorný et al. 2019). The similarity of compositions has been tested by both colors using HST (Benecchi et al. 2009), and recently with the NIRSpec spectrometer on the James Webb Space Telescope (JWST) (Souza-Feliciano et al. 2024), with all studies finding a similarity of spectra between binary components. Grundy et al. (2019) found that the known binary KBOs at the time indeed showed a prograde preference, and that preference is likely preserved even for wide binary KBOs after billions of years of solar perturbations on the binary orbit (Porter & Grundy 2012). There is thus considerable evidence to support the idea that CCKBOs were primarily formed through the SI, and primarily born as binaries, and that is the context we will use to analyze the shape and origin of Arrokoth.

(486958) Arrokoth was provisionally designated 2014 $MU_{69}$ and also called "PT1" and "Ultima Thule" prior to formal naming after the Powhatan word for Sky (in recognition of the traditional owners of the land on which the Johns Hopkins University Applied Physics Laboratory sits). It was discovered in 2014 with a deep survey using HST/WFC3 (Buie et al. 2024, for the full history of its discovery). Seen from Earth, Arrokoth appears very faint ($V \sim 26$; Benecchi et al. 2019) and is only reliably recoverable with HST for astrometry (Porter et al. 2018). Upon discovery it was immediately apparent from its orbital elements that Arrokoth was a CCKBO, and by early 2015, it was known to be the potential flyby target that required the smallest delta-v for targeting a New Horizons flyby. It was also clear that the flyby distance would have to be quite large if the orbit was only constrained by HST astrometry (Porter et al. 2018). The New Horizons mission then initiated a campaign to observe multiple stellar occultations by Arrokoth to provide high-precision astrometric points to constrain the KBO's orbit as well as measure its size, shape, and albedo (Buie et al. 2020). This campaign was uniquely enabled by access to the pre-release version of the ESA Gaia DR2 star catalog (Gaia Collaboration et al. 2018). The first attempt to observe a stellar occultation by Arrokoth on 3 June 2017 using telescopes in northern Argentina and South Africa was not successful. On 10 July 2017, the NASA/DLR Stratospheric Observatory for Infrared Astronomy (SOFIA) obtained a single, grazing occultation chord. From southern Argentina on 17 July 2017, the New Horizons occultation campaign finally successfully observed an Arrokoth occultation, obtaining five positive chords across the KBO (Buie et al. 2020). About one year later in August 2018, the campaign observed a second multi-chord stellar occultation by Arrokoth in Senegal (Buie et al. 2020). Together, these two occultations (along with HST data and the Gaia stars) provided an orbit solution with sufficiently high resolution that New Horizons was able to fly just 3536 km from Arrokoth and center the KBO within the full LORRI fov, thus revealing its shape in exquisite detail (Stern et al. 2019). However, even before the flyby, the occultations (especially the multi-chord event in 2017) revealed that Arrokoth has a complex shape. The 2017 occultation appeared to show two roughly circular objects, but it was not clear whether Arrokoth was a contact binary, a separated binary, or just an elongated object with large terrain relief (Buie et al. 2020). The post-flyby knowledge that Arrokoth is indeed a contact binary is strong motivation for conducting future stellar occultation studies of CCKBO shapes, as will be discussed below.

The New Horizons spacecraft first acquired Arrokoth on August 16 2018[1] with the LORRI (LOng Range Reconnaissance Imager; Cheng et al. 2008) camera in "4 × 4" photometric mode, but it showed no discernible lightcurve (Spencer et al. 2020). This was not surprising, as Arrokoth had shown no lightcurve to HST (Benecchi et al. 2019) and New Horizons was only looking 11° away from the Arrokoth-Earth direction. It was not until December 30, 2018, 2 days before the closest approach, that LORRI (in "1 × 1" high resolution imaging mode) was able to resolve the shape of Arrokoth, appearing to have bowling pin-like profile[2]. While further imaging continued, additional images were not downlinked to Earth until after the flyby on January 1, 2019. The first images returned after flyby (the "CA01" sequence) clearly showed the contact binary shape of Arrokoth. In total, 30 image sequences were returned that showed the resolved shape of Arrokoth, in addition to one ("CA07") that showed the double crescent of Arrokoth as New Horizons looked back at it with LORRI in 4 × 4 mode, as shown in Table 1. Arrokoth was the first and so far

[1] https://pluto.jhuapl.edu/News-Center/News-Article.php?page=20180828
[2] https://pluto.jhuapl.edu/News-Center/News-Article.php?page=20181231

only KBO to be imaged at sufficiently high resolution that its shape could be observed, and that shape was a contact binary comprised of two lenticular lobes, with little apparent surface topography apart from a very large crater (now named "Sky"). This is a shape unlike any other spacecraft target so far, but it is possibly indicative of a large fraction of KBOs formed by the Streaming Instability (McKinnon et al. 2020; Stern et al. 2023).

Preliminary versions of the shape model of Arrokoth published in Stern et al. (2019) and Spencer et al. (2020), both used a limited subset of the imagery and lacked variable albedo on the surface of Arrokoth. This latter point is important, as Arrokoth does show considerable albedo variation (by about a factor of two) around the interface between the lobes, in Sky Crater, and a few other features. The shape fitting program used for that analysis has been significantly improved through the support of the New Horizons Second Kuiper Belt Extended Mission (KEM2), and here we present the results of those improvements. In this work, we update the rotation period, shape, and pole solution of Arrokoth, and added albedo mapping of the imaged half of the body. We present updated estimates of the volumes of the lobes, and map out the terrain relief on the imaged hemispheres of the two lobes. We also discuss the implications of the updated shape model for the formation of Arrokoth in the context of the SI, as well as estimates of how frequent Arrokoth-like contact binaries may be in the Cold Classical Kuiper Belt. This work is also being prepared for submission to the NASA Planetary Data System (PDS), and here we provide documentation, context, and commentary on that product.

## 2. SHAPE FITTING

Fitting the shape of Arrokoth was challenging due to the extremely sparse dataset available. Arrokoth showed no discernible lightcurve in HST/WFC3 photometry (Benecchi et al. 2019), which (as we discuss below) is both likely why Arrokoth was discovered in the first place, and shows why the fraction of contact binaries in the Kuiper Belt could be presently underestimated (Showalter et al. 2021). This lack of a useful pre-flyby lightcurve meant that the rotational period of Arrokoth could only be constrained by New Horizons observations. However, even on approach to Arrokoth, the New Horizons photometric observations also showed no discernible lightcurve variation (Spencer et al. 2020). This is in contrast to the small satellites of Pluto, which did all show lightcurves on approach to Pluto, allowing their rotational periods to be constrained to high precision independently of their shapes or poles (Weaver et al. 2016; Porter et al. 2021). For Arrokoth, all constraints for shape, pole, and rotation rate would all have to come from the limited number of resolved images.

### 2.1. LORRI Image Analysis

New Horizons began obtaining images of Arrokoth on August 16, 2018, when the KBO was still much smaller than the 1.04 arcsecond pixels of LORRI (Weaver et al. 2020). LORRI is a 20.8 cm f/12.6 RC camera with $1024 \times 1024$ illuminated pixels on an E2V Technologies Model 47-20 CCD sensor (Cheng et al. 2008). LORRI has no filters, and its spectral response function (0.61 $\mu m$ pivot wavelength) is almost entirely determined by the CCD sensor (Cheng et al. 2008). The point spread function (PSF) of New Horizons LORRI is well-documented, and slightly asymmetric (Weaver et al. 2020). Arrokoth first became larger than the LORRI PSF on December 29, 2018, which was the first confirmation that it was not a separated binary (one possible interpretation of the occultation profile, Buie et al. 2020), but a rather single body. No satellites of Arrokoth were detected in these or any subsequent images during the flyby (Spencer et al. 2020).

The earliest images that usefully show the shape of Arrokoth were obtained on December 31, 2018, the day before the flyby. In total, 30 different resolved image sequences were useful for shape fitting, and they are listed in Table 1. Notably, only the southern half of Arrokoth was illuminated and visible in the LORRI images. The basic image analysis procedure was identical for all of the approach images, with some slight modification for the closest image sequence, CA06. Due to the desire to maximize the Jupiter gravity assist and reach Pluto as fast as possible, the New Horizons post-Pluto trajectory points roughly at $l=16°$, $b=-13°$ in galactic coordinates (Nelson et al. 2022). In practical terms, this means that the spacecraft is heading toward an extremely crowded star field near the galactic center, which both made the discovery of Arrokoth very challenging (Buie et al, under review), and also enabled the stellar occultations that first discovered its contact binary shape (Buie et al. 2020). A side effect of this trajectory is that even the very short exposure images of Arrokoth have detectable background stars. We were thus able to connect these stars to the Gaia DR3 catalog (Gaia Collaboration et al. 2023) and thus derive the absolute pointing of the images in the ICRF (International Celestial Reference Frame; Ma et al. 1998) frame. By combining this absolute pointing knowledge with the Arrokoth orbit determined from HST and occultation observations (Porter et al. 2018) and the trajectory of New
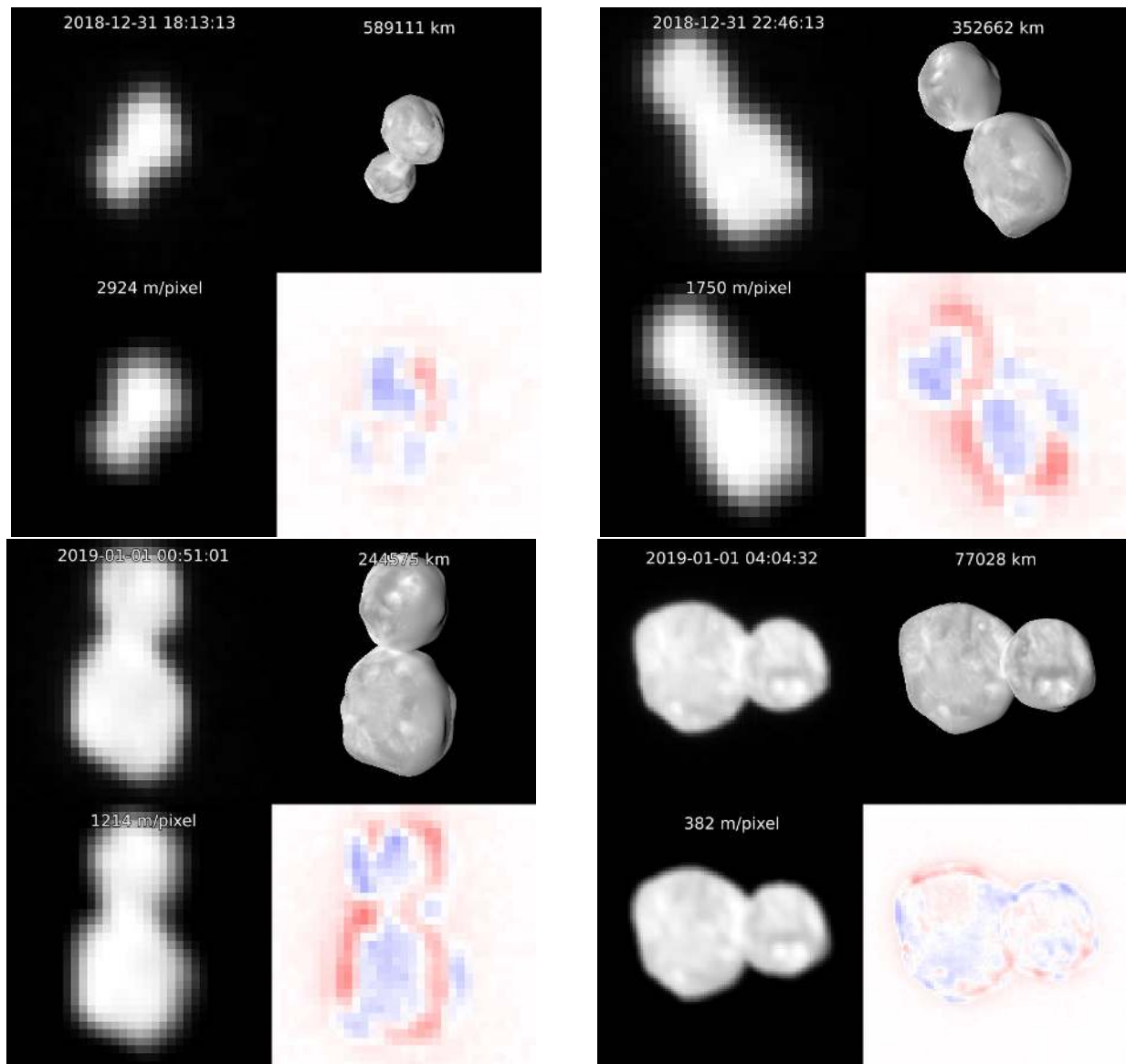
**Figure 1.** Four example distant images sequence stacks (`APROTNAV_L1_2018365A`,`APROTNAV_L1_2018365H`,`APROTNAV_L1_2019001C`, and `APROTNAV_L1_2019001K`) and their fit to the model. For each, the upper left shows the stacked, radiometrically-corrected image sequence obtained by LORRI, the upper right shows a high resolution render of the shape model with correct orientation and lighting, the lower left shows the shape model rendered at the resolution of the LORRI image and convolved with the LORRI PSF, and the lower right shows the difference between the images, blue for brighter in the the data, red for brighter in the synthetic image. The time of observation at the spacecraft, the distance between Arrokoth and the spacecraft, and the resolution of the image in kilometers per pixel are annotated in each image. Note that the distant and low-resolution images provide the strongest constraint on the shape of the "neck" between the two lobes.

Horizons as reconstructed from both optical navigation and radio data (Nelson et al. 2022), we can know exactly the ICRF geometry of each observation. This knowledge is critical for the following shape/pole analysis, and would be much more difficult to obtain without the Gaia-matched background stars. The images were radiometrically calibrated using the known LORRI radiometric calibration parameters (Weaver et al. 2020), converting them from instrument DN/second to "I/F", the ratio of sunlight reflected back to the detector, where I/F=1 is full reflectance and I/F=0 is no reflection. In order to maximize the signal-to-noise ratio (SNR) of the images, one image from each sequence was chosen as the fiducial, and the rest of the I/F-converted images are reprojected so that Arrokoth was in the same pixel position in all the images. These reprojected I/F images were then combined using a sigma-clipped median method
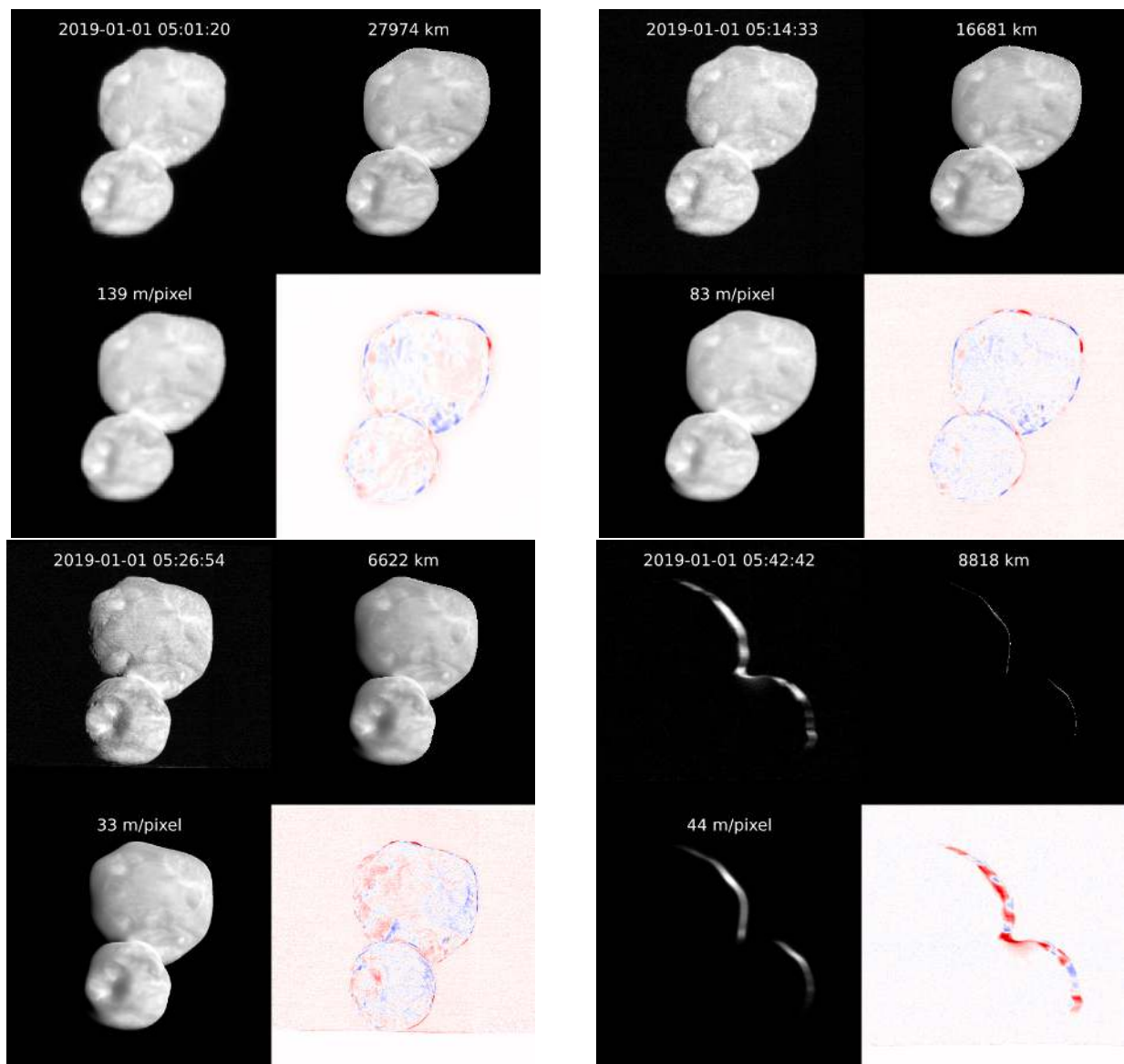
**Figure 2.** The closest four image sequences (CA04,CA05,CA06,CA07), in the same format as Figure 1. CA04 and CA05 are similar view angles, but CA05 is higher resolution, while CA04 was a deeper image sequence (and so less noisy). CA06 is the highest resolution image, and at considerably different phase angle (see Table 1). This meant that much of the fitting process was balancing the fit from CA06 with the fit for all the other images. CA07 is the only lookback image, and is considerably smeared (in the horizontal direction) by the motion of the spacecraft relative to Arrokoth as the 0.2 second exposures were taken.

(sigma-clipped stats in Astropy); this proved effective at filtering out cosmic rays, which were typically a larger source of noise in the images than CCD read noise. The resulting stacked images should then provide I/F images for each sequence with known geometry and the highest SNR possible. The image sequences and their particulars can be found in Table 1.

In addition to the imaging before close approach, New Horizons also obtained one useful "lookback" sequence (CA07) with the LORRI camera in $4 \times 4$ mode. This mode bins the illuminated $1024 \times 1024$ pixels on LORRI's sensor chip four by four, to produce a $256 \times 256$ image with pixels 4.16 arcseconds across on the sky (Cheng et al. 2008). The $4 \times$ mode allows for much deeper images than the unbinned $1 \times 1$ mode, and the loss of resolution is acceptable, as it is only slightly worse than the pointing stability of New Horizons under thrusters (New Horizons has no reaction wheels; Fountain et al. 2008). The CA07 sequence consisted of 336 total images with 0.2006 second exposure times, of which 13 contained the faint double crescent of Arrokoth. Like the $1 \times 1$ images, we registered each image to the Gaia DR3 stars
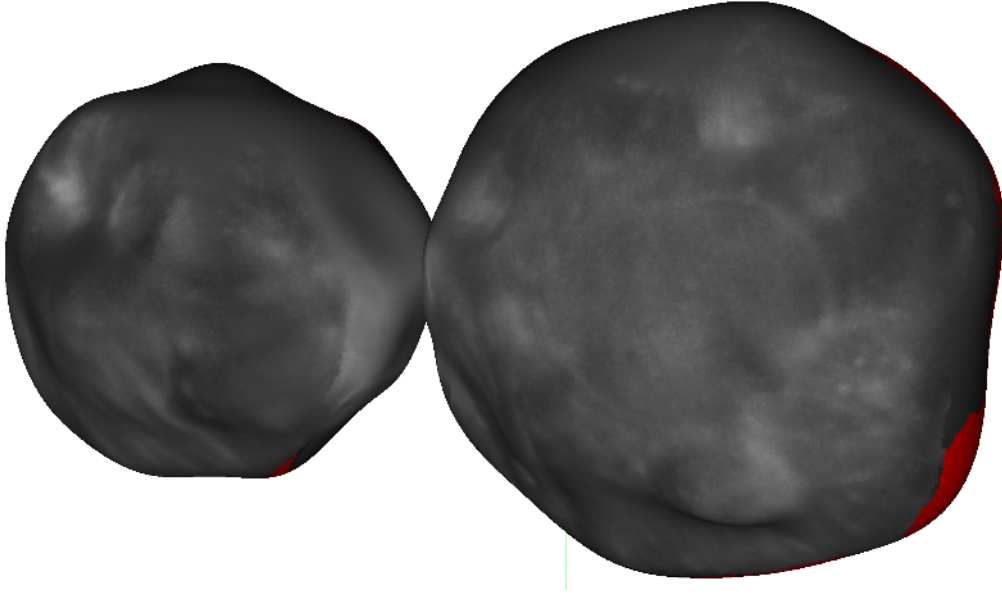
**Figure 3.** The shape model of Arrokoth as viewed from the negative (south) pole. Note the roughly hexagonal shape of Wenu, the larger lobe, and the similar (but less well-defined) hexagonal shape for Weeyo, the smaller lobe. This profile may be due to the formation of Arrokoth from "mounds", as detailed in (Stern et al. 2023). Note that the bright features in Akasa Linea (between the lobes) are relatively small, but appear relatively larger in the close approach images due to the viewing angle.

and used that to correct the WCS of the images. While the approach images were looking in the rough direction of the galactic center, the lookback images where looking opposite to that, still within the galactic plane and with plenty of stars for registration (indeed, substantially more than the $1 \times 1$s due to the longer exposure times). The images were then converted to I/F in the same way as the $1 \times 1$s, but using the $4 \times 4$ radiometric constants (Weaver et al. 2020).. The I/F images were then shifted and stacked to produce the final crescent image (see Figure 2). Because of the high solar phase angle (averaging 152°), the maximum I/F of the lookback image was only 0.0015, compared to 0.127 for the close approach images. This high-phase image also provided a strong constraint to the overall bidirectional reflectance function fit for the full object.

### 2.2. *Shape Fitting Analysis*

To simultaneously fit the shape, pole, and albedo, we used a forward-modeling method of rendering a parametric shape model and then attempting to find the best fit to the data. This forward-modeling method was required given the limited amount of data, and enabled a fit for the shape to be detailed on the imaged half of Arrokoth, while allowing detail on the unimaged half to be minimized. Forward-modeling that shape with a purely CPU-based approach would be time-consuming, and also unnecessary. We developed an OpenGL-based forward modeling process for modeling the shapes and poles of the small satellites of Pluto (which have even sparser datasets), as documented in Porter et al. (2021). This same method was used for the initial Arrokoth models published in Stern et al. (2019) and Spencer et al. (2020) and used for the analysis in McKinnon et al. (2020), Keane et al. (2022), and others. However, this shape fitting method had some key deficiencies, both in terms of the quality of its output and in the speed of execution of the code. The New Horizons KEM2 extended mission proposed to improve both the model and fitting technique to produce what would hopefully be the definitive shape model product for Arrokoth that is presented here.

The shape fitting model used here was effectively a rewrite of the older shape code to allow a transition from the PyOpenGL library to ModernGL[3]. ModernGL is a currently maintained OpenGL wrapper for Python 3 that implements many of the slower functions in C for speed. The shape fitting code is implemented as a Python script that is typically executed on the Linux command line, with command line arguments to define behavior. The shape fitter begins by creating a headless OpenGL context, which is useful to enable remote execution of the code. The OpenGL
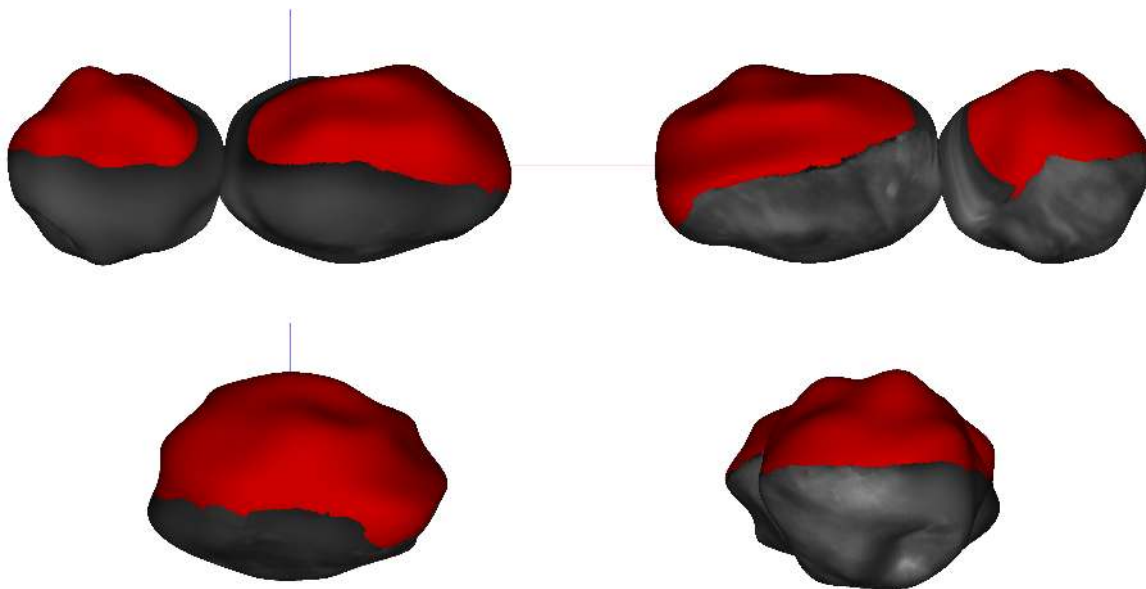
---

[3] https://moderngl.readthedocs.io/en/stable/index.html

**Figure 4.** The shape of Arrokoth as viewed from its equator. Red areas show regions that were not well-imaged by New Horizons. The detailed shape of these areas is effectively the reflections of the parametric shapes for the well-imaged parts (due to the nature of the octantoid spherical harmonics), though the overall dimensions are well constrained by the low resolution images (see Figure 1).

buffers for shape model and texture are defined here, and subsequent operations modify them without reallocation. The GLSL shaders are also defined and compiled here. There are two sets of shaders, a vertex and fragment shader to calculate the solar illumination on surface, and a vertex and fragment shader that calculate a shadow map, which is rendered directly to a texture. Next, a plain-text input file is read, which defines the rotational properties of the object, the parameterized shape, the photometric properties of the object (including if an albedo map is being used), and finally the input I/F images to fit. For Arrokoth, the overall shape was defined by two parametric shape models (one per lobe) and their offsets from center, though the code can use a single parameterized shape model as well. The lobes are parameterized with an "Octantoid" formalism as described by Kaasalainen & Viikinkoski (2012). This is similar to a spherical harmonic model, but has the advantage that the lowest-order parameters precisely define a triaxial ellipsoid. If an albedo map is defined, it is loaded in here; it is stored as floating point array in a FITS file. The map projection is also defined in the input file, which for Arrokoth was two south polar azimuthal equidistant maps (like the United Nations flag, but centered on the south pole), with a separate projection for each of the two lobes. This projection was chosen because it had the least amount of distortion for the high resolution images, and two separate projections were used to eliminate any ambiguities between the lobes. The script has predefined OpenGL UV maps for the supported map projections. The photometric parameters for the model are defined at this point too. This includes a a global albedo, which is multiplied by the albedo map if a map is used. Each of the images is defined with the input I/F FITS file (as produced with the procedure above), a number to define image type, and pixel x/y image offsets. Each of the I/F FITS files contain the observation time in SPICE Ephemeris Time (ET) at the spacecraft, the WCS-format pointing information, and the image data itself. The ET and WCS are used to create static OpenGL rotation and view matrices for each image. The image "mode" is used to define the PSF used for the image, with most of the images just using the native LORRI PSF, and with the CA07 images using a smeared LORRI PSF due to the spacecraft motion. Each image as allocated a fixed weight based on the square root of the number of images used in the stack divided by the spacecraft-target distance; this is required to ensure that the closest images don't entirely swap the more distant images that probe other parts of the shape.

With the input file read and processed, the script then performs the operation defined on the command line. The most central operation is to calculate the $\chi^2$ residuals for an input file or parameters. This starts with converting the parametric shape model from parameters to two closed, overlapping meshes. The evaluation of the spherical harmonics used the fast "lpmv" (associated Legendre function of integer order and real degree) function from SciPy (Virtanen

et al. 2020) using the CPU. The vertex normals are then calculated and used to define normals for each of the triangular facets. This facet normal calculation was one of the slowest parts of the older code, and in the new version is preformed in GPU using the PyOpenCL wrapper for OpenCL (Klöckner et al. 2009), allowing for considerable speedup. The updated vertices and normals are then copied to the appropriate OpenGL framebuffers. The photometric parameters are also copied over to the correct GPU variables for the shader to use. If the complexity flag was called in the input file, then the complexity factor is calculated here as the sum of the squares of all the shape parameters higher than first-order. If the balance flag was called in the input file, the volumes of the lobes are calculated and the offset of center of mass from the nominal center point is calculated. The script then integrates though each of the images. First, the object rotation matrix is calculated from the pole and rotation period, and this rotation matrix is applied to the pre-computed view matrix and the appropriate frame buffers updated. The synthetic image is then rendered with OpenGL. The GLSL shader uses the geometry provided to OpenGL to calculate the surface brightness with a bidirectional reflectance model (BDRM) of Hapke (2012). The shader uses the global photometric parameters and the albedo from the texture map to calculate the effective I/F for each pixel of the image. To define the functional form of the BDRM, we first used Equations 13 and 14 of Hapke (1981) to define a backscatter function:

$$B = (1 - \frac{tan|g|}{2h}(3 - exp(-\frac{h}{tan|g|}))(1 - exp(-\frac{h}{tan|g|})))exp(-\frac{w^2}{2}) \tag{1}$$

where $g$ is the Sun-Target-Observer phase angle in radians, $h$ is a parameter that defines particle spacing and was -7.05×$10^{-6}$ in the best fit, and $w$ is single-scattering albedo (as defined by the albedo map). Using Equation 14 of McGuire & Hapke (1995), we define a Double Henyey Greenstein function for the particle phase function as:

$$p_{HG} = \frac{1+c}{2}\frac{1-b^2}{(1-2b\ cos\ g+b^2)^{3/2}} + \frac{1-c}{2}\frac{1-b^2}{1+2b\ cos\ g+b^2} \tag{2}$$

where $c$ and $b$ are unitless parameters that define the shape of the phase function; $c$ was 0.564 and $b$ was 0.356 in the best fit. We also used the Ambartsumian-Chandrasekar H function approximation from Hapke (2012) Equation 8.56:

$$r_0 = \frac{1 - \sqrt{1-w}}{1 - \sqrt{1+w}} \tag{3}$$

$$H(x) \simeq 1/(1 - wx(r_0 + \frac{1}{2}(1 - 2r_0x)ln(\frac{1+x}{x})) \tag{4}$$

This is finally combined for a total BRDM function, Equation 16 of Hapke (1981):

$$r = \frac{\mu_{Sun}w}{\mu_{Sun} + \mu_{obs}}((1+B)p_{HG} + \mu_{sun}H(\mu_{Sun})H(\mu_{obs}) - 1) \tag{5}$$

where $\mu_{Sun}$ is the cosine of the angle between the surface normal and the direction of the Sun, and $\mu_{obs}$ is cosine of the angle between the surface normal and the direction of the observer. These functions were all directly implemented in GLSL, allowing them to be executed at speed in the GPU.

The rendered image is then copied from the GPU framebuffer back to CPU memory. Next, the image is convolved with the appropriate PSF. By default, this is done in CPU, but can be optionally performed by GPU using CUDA through Numba (Lam et al. 2015). The CUDA-based convolution generally executes much faster then in CPU, even with extra memory copies to and from the GPU. Finally, the rendered image is subtracted from the actual image, the difference image squared and summed, and multiplied by a weight based on the angular size of the object. This is calculated and summed for all the images, and the complexity and balance factors added if requested, and the result returned as the effective $\chi^2$ for optimization.

For the fit, the shape, pole, photometric properties, and individual image offsets can be allowed to vary. In practice, many iterations were performed with just one set of those parameters allowed to vary; a global parameter mask was set on the command line and the optimization functions only performed on the parameters in the mask. The available optimization functions included the SciPy implementations of the Powell (Powell 1964) and Nelder-Mead (Nelder & Mead 1965) function minimizers. The former optimizes parameters individually and is thus preferable for the shape and offsets, while the latter optimizes parameters all at once and is thus preferable for the highly covariant pole and photometric properties. In addition, two special optimizers were used, one of which only optimized the offsets individually, and another which only optimized the shape parameters one by one in order of absolute magnitude.

**Table 2.** Parameters of the best-fit shape solution.

|  | Full Body | Wenu | Weeyo |
|---|---|---|---|
| a Length | 34.546 km | 20.139 km | 15.041 km |
| b Length | 19.838 km | 19.838 km | 14.378 km |
| c Length | 13.822 km | 13.726 km | 13.625 km |
| a/b Ratio | 1.741 | 1.015 | 1.046 |
| a/c Ratio | 2.499 | 1.467 | 1.104 |
| Diameter of a Sphere of Equal Volume: | 19.896 km | 17.349 km | 13.845 km |
| Rotational Pole Right Ascension | 319.37° |  |  |
| Rotational Pole Declination | -25.588° |  |  |
| Pole inclination to heliocentric orbit | 100.39° |  |  |
| Pole inclination to approach direction | 41.096 deg° |  |  |

The "a" direction points from Weeyo to Wenu, the "c" direction points to the rotational pole, and "b" is mutually perpendicular.

This enabled a quick optimization that focused first on the parameters most relevant to the solution and could be be cancelled before spending time on the less important parameters. It was possible to capture incomplete solutions because the optimizer would output the current state after optimizing each parameter. This could then be fed back into the command line using a flag that looked for parameters in STDIN, and could plot or save those parameters into an input file. The models could be visually inspected with a separate script that transformed the parametric model into a mesh and displayed it in an interactive way using Vispy (Campagnola et al. 2022); this script was also used to generate Figures 3 and 4.

A low-order model (essentially two triaxial ellipsoids) was initially used, and then more orders were gradually added on to increase the complexity, with the final model using order-9 octantoids. Once a good initial model with uniform albedo converged, it was used to fit an albedo map, and then refit with the albedo map, the map refit, and so on. The albedo map was produced by first reprojecting the 30 approach images using the shape model, saving both the I/F brightness and the angles needed for the bidirectional reflectance model (BDRM). A best-fit was then found for the albedo map using the reprojected images, weighted for the original resolution of the reprojected image. This method allowed us to combine all the images, both the high resolution close approach images that showed detail on the surface and the more distant images that showed other aspects of the shape, to be combined into one albedo map. Fitting the shape and albedo map was a highly iterative process, which took nearly a year to finally converge on a best fit shape. The initial model developed after flyby had an incorrect pole and did not model the variability in surface albedo, resulting a much flatter shape, and which had no constraints on the unlit side of Arrokoth. This model was published in Spencer et al. (2020) and in the original PDS delivery. The current model corrects the pole and recenters the shape, to be roughly balanced volumetrically, and (as noted below) this has a significant impact on the interpretation of the model.

## 3. SHAPE FITTING RESULTS

Comparison plots between the LORRI data and the model can be seen in Figures 1 and 2, orthographic projections of the shape model are shown in Figures 3 and 4, and the parameters of its shape and pole listed in Table 2. The model itself is included in the supplementary material as an OBJ file. Note that since not all of the shape was seen by New Horizons, the red areas are used in Figures 3 and 4 to denote areas that were not imaged by New Horizons and only constrained by their absence. The overall shape is bilobate, with the small lobe Weeyo being roughly spherical, and the large lobe Wenu being significantly oblate. Neither lobe is particularly prolate, although Weeyo is slightly more prolate, and its long axis is aligned to point at Wenu. Weeyo contacts Wenu along the equator of Wenu, though the exact contact point is obscured in the high resolution images (see Figure 1 for the best image constraint on the
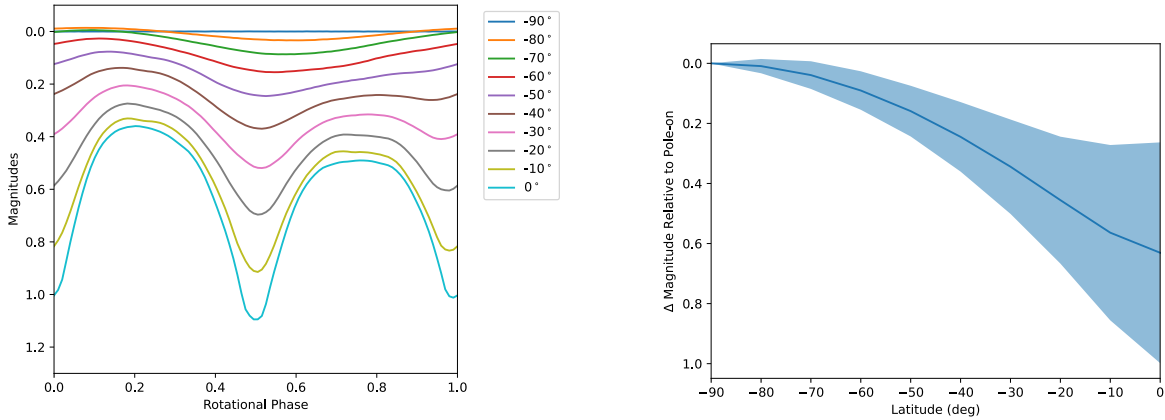
**Figure 5.** The rotation lightcurve of Arrokoth at a Sun-Target-Observer angle of zero, as viewed from various sub-observer latitudes. The left plot shows the variation in the shape and reflectance of the lightcurve at different latitudes, while the right plot shows the variation of the mean reflectance and lightcurve amplitude as a function of sub-observer latitude. Note the flattened shape of the two lobes of Arrokoth mean that the low latitudes (which show any amount of lightcurve variation) are also more than a half magnitude fainter on average than the mean reflectance when viewed pole-on. This is significantly different from the results of Showalter et al. (2021), and can substantially affect the statistics of discovered KBOs.

neck). The apparent volume ratio between Wenu and Weeyo is 1.967:1; though the precise value could vary based on the unseen areas on the unlit side of Arrokoth, it cannot vary too much from 2:1 without being invalidated by the approach images. The overall body is much more elongated and flattened than the individual lobes, and this is reflected its rotation lightcurve shown in Figure 5.

Both lobes appear to be roughly hexagonal in shape along their equators, with Weeyo's long axis aligned to its contact point with Wenu, while Wenu appears somewhat misaligned as viewed from the pole (see Figure 3). This contact region, named Akasa Linea, appears to be filled with high albedo material (Hofgartner et al. 2021), which obscures the shape information and makes fitting the shape of the contact region difficult. Overall the nominal albedo of the body (using the BDRF described above) varies from ∼0.017 to ∼0.08, with the bright albedo features found in discrete areas on both lobes, notably inside Sky Crater on Weeyo, Akasa, and several areas of Wenu, including the circular Ka'an Arcus feature in the center of Wenu. Ka'an Arcus appears to encircle an area of elevated terrain, consistent with it being a separate "mound" (as proposed by Stern et al. 2023, see Figure 4). The overall profile of Wenu is more similar to cylindrical prism than a perfect triaxial ellipsoid, with near-vertical sides topped by a flat surface with a raised central mound (see Figure 4). In contrast, Weeyo appears to be close to a spherical object with significant surface terrain dominated by Sky Crater.

The fitting methods used here were not perfect, and they did not fully fit the shape and albedo to the limits of the data. A notable deficiency is the area of Wenu closest to Akasa which hosts a small bright albedo feature. This area never quite converged, and the residuals of this poor fit stand out in Figure 2. Also, the full shape of Sky Crater is below the resolution of the parametric model, particularly along the rim. This is also true of all of the small craters that are visible near the terminator. In general, however, the overall shape of Arrokoth was well fit by the model. Future work is planned to use this low-frequency model as a basis for higher resolution stereophotoclinometry of the well-imaged parts of the surface.

## 4. DISCUSSION

### 4.1. *On the Frequency of Contact Binaries in the Kuiper Belt*

The synthetic rotation lightcurve of Arrokoth projected at various sub-observer latitudes is shown on the left in Figure 5, and the amount of lightcurve variation, or amplitude, as a function of sub-observer latitude is shown on the right in Figure 5. These figures were created with the same forward-modeling code as described above, but with a fictional observer looking at the shape at precisely solar opposition (i.e. Sun-Target-Observer angle of zero), and then taking the sum of the rendered image pixels to produce an effective reflectance for each point in the lightcurve. This is done for 11 different longitudes to produce the effective zero-phase lightcurves shown in Figure 5. Therefore, the amplitudes of the rotation lightcurves of an Arrokoth-shaped object can vary greatly, depending on the sub-observer

latitude. Notably, seen from Earth, the sub-observer latitude on Arrokoth is closest to the -80° line, thus showing why no rotation lightcurve amplitude for it was found in HST photometry (Benecchi et al. 2019).

The discovery of Arrokoth by HST was enabled by its low-amplitude rotation lightcurve, as it was just barely visible in HST's WFC3 (roughly 144 photons per 350 second image; Benecchi et al. 2019). In general most KBOs do not have lightcurves with large amplitudes, and as succeeding surveys try to probe deeper, they can only consider objects thatcan be consistently recovered at close to the minimum detectable brightness for the survey (e.g. Fraser et al. 2024, submitted). This situation is compounded by the fact that objects with a consistent brightness are much more likely to have the required multiple-opposition follow up observations that enable targeted lightcurve follow-up. This has likely led to a considerable bias in the documented KBO rotation lightcurves towards objects that do not reveal any shape information. Showalter et al. (2021) recognized this bias shortly after the Arrokoth flyby, but their analysis was based on the idea that Arrokoth's shape was approximated by two spheres in contact with each other. As Figure 5 shows, this effect is even more pronounced for the actual flattened contact binary shape of Arrokoth. Lightcurve-based estimates of contact binary frequency (e.g. Thirouin & Sheppard 2019) therefore may be considerably underestimating the frequency of contact binaries in the Kuiper Belt. The Vera Rubin Observatory (soon to come online at time of publication) offers a potential antidote to this bias, as its wide and deep ecliptic plane survey (Schwamb et al. 2023) may be able recover faint KBOs of variable brightness, and then offer a regular cadence of observations to detect that lightcurve variation. Arrokoth is a very typical Cold Classical KBO in its orbital characteristics (Porter et al. 2018), and future KBO lightcurve studies should seek to test if it is typical in shape as well. Porter et al. (2022) presents several KBOs that were observed by New Horizons at high solar phase angles and are good candidates to perform this test.

### 4.2. *Implications for Formation*

The shapes of the two lobes of Arrokoth are particularly interesting because they must have formed separately and later come together to form the contact binary shape (McKinnon et al. 2020). As noted in the introduction, the dominant theory for the formation of KBOs is through the SI, which can rapidly collapse dust from the circumsolar disk into solid bodies (Carrera et al. 2017), many of them them initially in loosely bound binary orbits (Nesvorný et al. 2019). Stern et al. (2023) have shown that this process can accrete objects in such a way that results in bodies seeming to form "mounds", and the shape model presented here is fully consistent with that process. McKinnon et al. (2020) proposed that the two components of Arrokoth were initially on a bound orbit and came together under gas drag, allowing their mutual orbit semi-major axes to gradually decay until they reached a soft contact. Nothing in the shape model presented here is inconsistent with that proposal, including the relatively small contact point between the lobes that suggests a very gentle process for bringing them together.

The shape model presented here does present some new questions and constraints for formation models. The hexagonal shape of both lobes is extremely curious and is not completely explained by the "Mounds Model" (Stern et al. 2023). Both lobes being roughly similar size on their shortest axis is also intriguing, and may point to them forming out of a more disk-like structure of that thickness, but such a conclusion requires future modeling. The raised central mound on Wenu likely also points to a feature of formation, possibly that Wenu originally formed as a more spherical object before accreting the material on its equator. But again, that possibility would require future formation modeling to fully understand. The presented shape model also provides a powerful test for any alternative KBO formation models to the SI. The complex shape of Arrokoth being so well explained by the SI means that any alternative theories would need to be able to reproduce Arrokoth-like shapes as least as well as the SI.

### 5. CONCLUSIONS

The updated shape model of Arrokoth provides a much better basis for understanding this small distant world than previous shape models. The updated, thicker shape model is more consistent with formation though the Streaming Instability (Nesvorný et al. 2019; Stern et al. 2023), while still being consistent with proposed models for how the two components of Arrokoth came together (McKinnon et al. 2020). The volume ratio of almost precisely 2:1 between the two lobes is intriguing and should provide interesting constraints for future formation modeling efforts. The updated shape model includes a significant decrease in reflectance as seen from the equator, which is strong evidence that the contact binary population in the Kuiper Belt may be significantly underestimated. Arrokoth is fascinating both because it is unlike any other object ever visited by a spacecraft and because it could be an archetype for thousands of KBOs yet to be explored.

## REFERENCES

Abod, C. P., Simon, J. B., Li, R., et al. 2019, ApJ, 883, 192, doi: 10.3847/1538-4357/ab40a3

Annex, A., Pearson, B., Seignovert, B., et al. 2021, AndrewAnnex/SpiceyPy: SpiceyPy 4.0.1, v4.0.1, Zenodo, doi: 10.5281/zenodo.4883901

Astropy Collaboration, Price-Whelan, A. M., Lim, P. L., et al. 2022, ApJ, 935, 167, doi: 10.3847/1538-4357/ac7c74

Benecchi, S. D., Noll, K. S., Grundy, W. M., et al. 2009, Icarus, 200, 292, doi: 10.1016/j.icarus.2008.10.025

Benecchi, S. D., Noll, K. S., Grundy, W. M., & Levison, H. F. 2010, Icarus, 207, 978, doi: 10.1016/j.icarus.2009.12.017

Benecchi, S. D., Noll, K. S., Stephens, D. C., Grundy, W. M., & Rawlins, J. 2011, Icarus, 213, 693, doi: 10.1016/j.icarus.2011.03.005

Benecchi, S. D., Porter, S. B., Buie, M. W., et al. 2019, Icarus, 334, 11, doi: 10.1016/j.icarus.2019.01.023

Buie, M. W., Porter, S. B., Tamblyn, P., et al. 2020, AJ, 159, 130, doi: 10.3847/1538-3881/ab6ced

Buie, M. W., Spencer, J. R., Porter, S. B., et al. 2024, arXiv e-prints, arXiv:2403.04927, doi: 10.48550/arXiv.2403.04927

Campagnola, L., Larson, E., Klein, A., et al. 2022, vispy/vispy: Version 0.11.0, v0.11.0, Zenodo, doi: 10.5281/zenodo.6795163

Carrera, D., Gorti, U., Johansen, A., & Davies, M. B. 2017, ApJ, 839, 16, doi: 10.3847/1538-4357/aa6932

Cheng, A. F., Weaver, H. A., Conard, S. J., et al. 2008, SSRv, 140, 189, doi: 10.1007/s11214-007-9271-6

Edgeworth, K. E. 1949, MNRAS, 109, 600, doi: 10.1093/mnras/109.5.600

Elliot, J. L., Kern, S. D., Clancy, K. B., et al. 2005, AJ, 129, 1117, doi: 10.1086/427395

Fountain, G. H., Kusnierkiewicz, D. Y., Hersman, C. B., et al. 2008, SSRv, 140, 23, doi: 10.1007/s11214-008-9374-8

Fraser, W. C., Bannister, M. T., Pike, R. E., et al. 2017, Nature Astronomy, 1, 0088, doi: 10.1038/s41550-017-0088

Gaia Collaboration, Brown, A. G. A., Vallenari, A., et al. 2018, A&A, 616, A1, doi: 10.1051/0004-6361/201833051

Gaia Collaboration, Vallenari, A., Brown, A. G. A., et al. 2023, A&A, 674, A1, doi: 10.1051/0004-6361/202243940

Goldreich, P., Lithwick, Y., & Sari, R. 2002, Nature, 420, 643, doi: 10.1038/nature01227

Greenstreet, S., Gladman, B., McKinnon, W. B., Kavelaars, J. J., & Singer, K. N. 2019, ApJL, 872, L5, doi: 10.3847/2041-8213/ab01db

Grundy, W. M., Noll, K. S., Roe, H. G., et al. 2019, Icarus, 334, 62, doi: 10.1016/j.icarus.2019.03.035

Hapke, B. 1981, J. Geophys. Res., 86, 3039, doi: 10.1029/JB086iB04p03039

—. 2012, Theory of Reflectance and Emittance Spectroscopy, doi: 10.1017/CBO9781139025683

Hofgartner, J. D., Buratti, B. J., Benecchi, S. D., et al. 2021, Icarus, 356, 113723, doi: 10.1016/j.icarus.2020.113723

Jewitt, D., & Luu, J. 1993, Nature, 362, 730, doi: 10.1038/362730a0

Kaasalainen, M., & Viikinkoski, M. 2012, A&A, 543, A97, doi: 10.1051/0004-6361/201219267

Keane, J. T., Porter, S. B., Beyer, R. A., et al. 2022, Journal of Geophysical Research (Planets), 127, e07068, doi: 10.1029/2021JE007068

Klöckner, A., Pinto, N., Lee, Y., et al. 2009, arXiv e-prints, arXiv:0911.3456, doi: 10.48550/arXiv.0911.3456

Kuiper, G. P. 1974, Celestial Mechanics, 9, 321, doi: 10.1007/BF01228575

Lam, S. K., Pitrou, A., & Seibert, S. 2015, in Proc. Second Workshop on the LLVM Compiler Infrastructure in HPC, 1–6, doi: 10.1145/2833157.2833162

Leiva, R., Buie, M. W., Keller, J. M., et al. 2020, PSJ, 1, 48, doi: 10.3847/PSJ/abb23d

Ma, C., Arias, E. F., Eubanks, T. M., et al. 1998, AJ, 116, 516, doi: 10.1086/300408

McGuire, A. F., & Hapke, B. W. 1995, Icarus, 113, 134, doi: 10.1006/icar.1995.1012

McKinnon, W. B., Richardson, D. C., Marohnic, J. C., et al. 2020, Science, 367, aay6620, doi: 10.1126/science.aay6620

Nelder, J. A., & Mead, R. 1965, The computer journal, 7, 308, doi: 10.1093/comjnl/7.4.308

Nelsen, M. A., Ragozzine, D., Proudfoot, B. C. N., Giforos, W. G., & Grundy, W. 2024, arXiv e-prints, arXiv:2403.12786, doi: 10.48550/arXiv.2403.12786

Nelson, D. S., Pelletier, F. J., Buie, M. W., et al. 2022, SSRv, 218, 11, doi: 10.1007/s11214-022-00877-4

Nesvorný, D., Li, R., Youdin, A. N., Simon, J. B., & Grundy, W. M. 2019, Nature Astronomy, 3, 808, doi: 10.1038/s41550-019-0806-z

Porter, S. B., & Grundy, W. M. 2012, Icarus, 220, 947, doi: 10.1016/j.icarus.2012.06.034

Porter, S. B., Verbiscer, A. J., Weaver, H. A., Cook, J. C., & Grundy, W. M. 2021, in The Pluto System After New Horizons, ed. S. A. Stern, J. M. Moore, W. M. Grundy, L. A. Young, & R. P. Binzel, 457–472, doi: 10.2458/azu_uapress_9780816540945-ch020.

Porter, S. B., Buie, M. W., Parker, A. H., et al. 2018, AJ, 156, 20, doi: 10.3847/1538-3881/aac2e1

Porter, S. B., Spencer, J. R., Verbiscer, A., et al. 2022, PSJ, 3, 23, doi: 10.3847/PSJ/ac3491

Powell, M. J. 1964, The computer journal, 7, 155, doi: 10.1093/comjnl/7.2.155

Schwamb, M. E., Jones, R. L., Yoachim, P., et al. 2023, ApJS, 266, 22, doi: 10.3847/1538-4365/acc173

Showalter, M. R., Benecchi, S. D., Buie, M. W., et al. 2021, Icarus, 356, 114098, doi: 10.1016/j.icarus.2020.114098

Souza-Feliciano, A. C., Holler, B. J., Pinilla-Alonso, N., et al. 2024, A&A, 681, L17, doi: 10.1051/0004-6361/202348222

Spencer, J. R., Stern, S. A., Moore, J. M., et al. 2020, Science, 367, aay3999, doi: 10.1126/science.aay3999

Stern, S. A., Weaver, H. A., Spencer, J. R., et al. 2019, Science, 364, aaw9771, doi: 10.1126/science.aaw9771

Stern, S. A., White, O. L., Grundy, W. M., et al. 2023, PSJ, 4, 176, doi: 10.3847/PSJ/acf317

Thirouin, A., & Sheppard, S. S. 2019, AJ, 157, 228, doi: 10.3847/1538-3881/ab18a9

Tsiganis, K., Gomes, R., Morbidelli, A., & Levison, H. F. 2005, Nature, 435, 459, doi: 10.1038/nature03539

Virtanen, P., Gommers, R., Oliphant, T. E., et al. 2020, Nature Methods, 17, 261, doi: 10.1038/s41592-019-0686-2

Weaver, H. A., Porter, S. B., Spencer, J. R., & The New Horizons Science Team. 2022, PSJ, 3, 46, doi: 10.3847/PSJ/ac4cb7

Weaver, H. A., Buie, M. W., Buratti, B. J., et al. 2016, Science, 351, aae0030, doi: 10.1126/science.aae0030

Weaver, H. A., Cheng, A. F., Morgan, F., et al. 2020, PASP, 132, 035003, doi: 10.1088/1538-3873/ab67ec

Youdin, A., & Johansen, A. 2007, ApJ, 662, 613, doi: 10.1086/516729